Valley anisotropy in elastic metamaterials

Shuaifeng Li,[1,2] Ingi Kim,[3] Satoshi Iwamoto,[3] Jianfeng Zang ⬤,[2,*] and Jinkyu Yang[1,†]

[1]*Department of Aeronautics and Astronautics, University of Washington, Seattle, Washington, 98195-2400, USA*
[2]*School of Optical and Electronic Information and Wuhan National Laboratory for Optoelectronics,*
Huazhong University of Science and Technology, Wuhan, Hubei, 430074, China
[3]*Institute of Industrial Science, The University of Tokyo, Meguro, Tokyo, 153-8505, Japan*

Valley, as a degree of freedom, raises the valleytronics and classical analogs in fundamental and applied science. Here, by designing asymmetrical elastic metamaterials made of hard and soft materials, we present the valley anisotropy that has not been explored in conventional symmetric systems. We demonstrate the creation of valley topological insulators by tuning an anisotropic Berry curvature and show topological waves relying on operating frequencies. The proposed topological properties can contribute to better understanding the valley topology and to creating a different type of topological insulator.

I. INTRODUCTION

Elastic waves possess plenty of degree of freedoms (DOFs), including frequencies, phases, and polarizations, thus enabling a variety of applications such as target detection, information processing, nondestructive evaluation, structural health monitoring, acoustic lens, energy focusing, and biomedical imaging [1–7]. Recently, topology has been proposed as a new DOF in manipulating waves in both photonic and phononic systems. This new tool exhibits remarkable impact not only on fundamental science such as condensed matter physics, but also on engineering applications, e.g., low loss devices and waveguides [8–12]. In photonics, the photonic spin Hall effect has been achieved by taking advantage of spin DOF, which opens up an avenue of spin-dependent light transport and one-way spin transport [13–16]. In phononics, mechanical patterns and deformations have been employed as mechanisms to enable the elastic topological states [11,12,17–24].

Recently, valley—the degenerate yet inequivalent energy extrema in momentum space— has emerged as a dimension in manipulating waves in electronics, photonics, and phononics [8,9,25–31]. In graphene and transition metal dichalcogenides (TMD), the valley Hall effect has been studied for the promising applications in information carrier and storage [27,29–31]. As the concept of valley is introduced into the classic system, the photonic and phononic valley crystals have also been proposed, showing valley-dependent energy transportation [8,9,25,26,28]. Likewise, various designs of elastic valley metamaterials have been reported based largely on the two different types: TMD-inspired hexagonal lattices, and triangular lattices with triangle-like scatterers [11,12,25,26,32,33]. However, existing designs of valley metamaterials are limited

to the inherent spatial inversion symmetry of the physical system, in which the typical Berry curvature distribution follows $\Omega(-\boldsymbol{k}) = \Omega(\boldsymbol{k})$ where $\boldsymbol{k}$ is a wave vector in the Brillouin zone. The valley metamaterials without spatial inversion symmetry have not yet been explored. The introduction of asymmetrical design into valley metamaterials may add an additional DOF in manipulating waves for wave guiding and information carrying purposes.

In this manuscript, we report a concept of valley anisotropy by introducing asymmetrical architectures into elastic metamaterials. The proposed elastic valley metamaterials are composed of hard spiral scatterers and soft material matrix. The spiral structure ensures the system without spatial inversion symmetry. The valley anisotropy is revealed by the exceptional Berry curvature of this chiral anisotropic system. We show that the Berry curvature can be tuned by adjusting the geometrical parameters of spiral scatterers. By leveraging this enhanced design freedom, we demonstrate that our asymmetrical design enables unprecedented topological manipulation of transverse elastic waves, allowing bending and stoppage of energy flow. Such manipulation of transverse waves can be useful in high-resolution imaging, such as trans-skull measurement and treatment in biomedical systems because of their high penetration and contrast characteristics in human body [2,4,34]. The elastic valley states, carrying notable features of vortices, may also inspire different engineering applications in energy harvesting, vibration filtering, and impact mitigation.

II. ELASTIC VALLEY METAMATERIALS DESIGN

The proposed elastic valley metamaterials are designed in a triangular lattice using the hard spirals made of polylactic acid (PLA) as scatterers and the soft hydrogel as the matrix [Figs. 1(a) and 1(b)]. Hydrogels are chosen as the soft matrix, which are acoustically similar to water and are ideally biocompatible materials [35]. The spiral element is

*Corresponding author: jfzang@hust.edu.cn
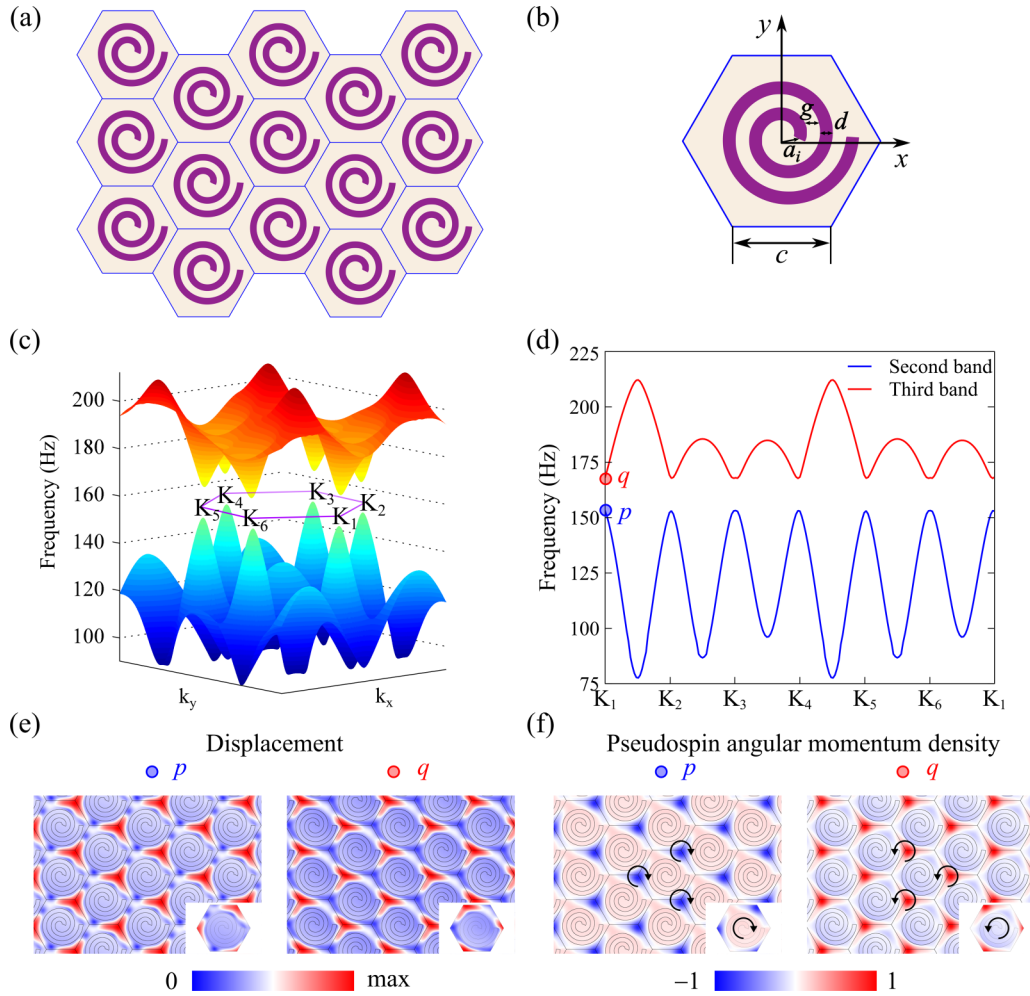†Corresponding author: jkyang@aa.washington.edu

FIG. 1. (a) Schematics of the elastic valley metamaterial in the triangle lattice. The Archimedean spiral-like structure is employed as the hard scatterer shown in purple. The soft hydrogel matrix is shown in beige. (b) The unit cell with detailed design parameters. (c) The band structure of the first Brillouin zone (purple lines with six corners marked by K_1, K_2, K_3, K_4, K_5, and K_6) with the second and the third bands showing the valley characteristic. (d) The band structure along the edge of the first Brillouin zone. The blue (red) curve represents the second (third) band. The two states in the K_1 valley are denoted as p and q states. (e) The displacement field distributions of p and q valley states. The insets show the displacement field of the unit cell. (f) The normalized pseudospin angular momentum density distributions of p and q valley states. The insets show the displacement field of the unit cell. The curved arrows indicate the pseudospin up and pseudospin down.

in the low order of symmetry falling into the point group C_s that only contains identity and σ_{xy} symmetries. This ensures the asymmetrical elastic valley metamaterial [36]. As a typical example in the monofilar spiral, the Archimedean spiral structure is employed in our design of the unit cell. The mechanical properties for spiral PLA are: mass density 1250 kg/m³, Young's modulus 2.1 GPa, and Poisson's ratio 0.36. The geometric parameters of the spiral are defined in Fig. 1(b), in which initial spiral radius $a_i = 1.5$ mm, gap distance $g = 2.25$ mm, thickness of the spiral $d = 2$ mm, and the number of turns $n = 2$. The mechanical properties of soft hydrogels are: mass density 1000 kg/m³, Young's modulus 18 kPa, and Poisson's ratio 0.5. The side dimension of the hexagon is $c = 14$ mm.

We conduct the finite element analysis of the spiral system under the plane-strain condition using Comsol Multiphysics. Figure 1(c) presents the band structure of the first Brillouin zone with the second and the third transverse wave bands separated by an omnidirectional band gap. In contrast to the

Dirac dispersion in lattices with C_{3v} symmetry, the band gap in our spiral system is a result of breaking the symmetry between the lattice and the scatterers, which is guaranteed by the asymmetric spiral structure in our design. Because of the chiral structure, we use six symbols from K_1 to K_6 to present the corners of the Brillouin zone. We illustrate the two bands along the edge of the first Brillouin zone (i.e., from K_1 to K_6) in Fig. 1(d). We find that the both bands between K_1 and K_2 valleys are different from those between K_2 and K_3 valleys, and between K_3 and K_4. According to the translational symmetry, there exist two inequivalent valleys, and Figs. 1(c) and 1(d) verify the anisotropic band structure in our spiral structure.

We further investigate the elastic valley states of the spiral structure in the eigendisplacement field and valley polarizations. We choose p and q of the second and third bands at K_1 valley as two representing elastic valley states, as marked in Fig. 1(d). Similar to electronic valley states as well as the photonic and acoustic valley states, elastic valley states also exhibit a notable chirality, as shown in the

eigendisplacement field of the p and q states in Fig. 1(e). Figure 1(f) illustrates the normalized pseudospin angular momentum density of phonons in the p and q states, which is defined as $S = \frac{\rho \omega}{2} \langle u | \hat{S} | u \rangle$, where ρ is the mass density, ω is the angular frequency, u is the eigendisplacement field, and $\hat{S}$ is the spin-1 operator [37]. It can be simplified to $S = \frac{\rho}{2\omega} Im(v^* \times v)$, which indicates the rotation of the velocity field. The local particle rotates clockwise or counterclockwise driven by the phase difference. For convenience, we define the clockwise and the counterclockwise rotations as pseudospin-down and pseudospin-up based on the right-hand rule [see the arrows in Fig. 1(f)].

The pseudospin angular momentum characterizes the polarizations of phonons, e.g., linear, elliptical, and circular polarizations. In the analysis of valley polarization, we find the p and q states exhibit different polarizations. For example, when we investigate the p state, we find that the pseudospin angular momentum density concentrates mainly in the three corners of the hexagon, where the normalized pseudospin angular momenta exhibit a negative unity, indicating the circular polarizations in the pseudospin-down state [see the left inset in Fig. 1(f)]. In stark contrast, the q state exhibits the pseudospin-up state in a different set of corners [right inset of Fig. 1(f)]. It is interesting to note that the p state exhibits circular (linear or elliptical) polarization at the three corners of hexagon, where the q state exhibits linear or elliptical (circular) polarization with the opposite pseudospin angular momentum. This implies that the p and q states have opposite chirality, manifesting that our anisotropic system presents valley features.

We note in passing that the combined landscape of the displacement field distribution and the normalized pseudospin angular momentum distribution is different from the existing valley states in classic systems. In our system, the amplitudes of both the displacement field and the normalized pseudospin angular momentum field reach maximum at the identical corners of the hexagon [compare Figs. 1(e) and 1(f)]. In classical systems, however, the normalized pseudospin angular momentum reaches a maximum at the position where the field amplitude becomes zero (see the Appendix for comparison). The observed anomalous valley states have never been reported in the classic systems, which can enrich the intrinsic physics of valley states.

III. BERRY CURVATURE AND VALLEY CHERN NUMBER

Now we explore the topology of the valley in the observed anisotropic band structure. After obtaining the dispersion relation $\omega = \omega(\mathbf{k})$ and displacement vector field $\mathbf{U}(\mathbf{k})$, we characterize the topology of valley by calculating the Berry curvature $\Omega(\mathbf{k}) = i\nabla_{\mathbf{k}} \times \langle u(\mathbf{k}) | \nabla_{\mathbf{k}} | u(\mathbf{k}) \rangle$, where $\nabla_k = (\partial_{k_x}, \partial_{k_y})$ using the discrete method [38]. For our two-dimensional system, we consider a clockwise path around a certain point $A(k_x, k_y)$ consisting of $A_1(k_x - \delta k_x/2, k_y - \delta k_y/2)$, $A_2(k_x - \delta k_x/2, k_y + \delta k_y/2)$, $A_3(k_x + \delta k_x/2, k_y + \delta k_y/2)$, and $A_4(k_x + \delta k_x/2, k_y - \delta k_y/2)$. According to the definition and the Stokes' theorem, we obtain $\int \Omega d^2 k = -\int \mathbf{B} \cdot d\mathbf{k}$, where $\mathbf{B}$ is the Berry potential of a state defined by $\langle iU_k | \nabla_k U_k \rangle$. Since we consider the continuous Brillouin zone as numerous small patches, for each patch $\delta k_x \times \delta k_y$, we estimate the Berry curvature as below:

$$\Omega(A) = \frac{Im[\langle U(A_1) | U(A_2) \rangle + \langle U(A_2) | U(A_3) \rangle + \langle U(A_3) | U(A_4) \rangle + \langle U(A_4) | U(A_1) \rangle]}{\delta k_x \times \delta k_y},$$

where the inner product can be calculated using Comsol Multiphysics. This equation can be justified when patches are much smaller than the first Brillouin zone. In our case, $\delta k_x = \delta k_y = 3.74 \, m^{-1}$ and the side length of the first Brillouin zone is $172.74 \, m^{-1}$, hence this method is reasonable. Then, we can map the Berry curvature of the Brillion zone, which will be presented below for further discussion.

For an elastic system with the time reversal symmetry, the integration of the Berry curvature of the whole Brillouin zone is expected to be zero. Nevertheless, the Berry curvature is highly localized at the valleys, and the local integration of the Berry curvature converges to a nonzero quantized value. The local integration is referred to as valley Chern number C_v, which is defined as $C_v = \frac{1}{2\pi} \int \Omega(\mathbf{k}) d^2 \mathbf{k}$, where the integral bounds extend to a local area around the valley. In the existing valley physics, C_v is calculated to be $\pm 1/2$ in electronic, photonic, and phononic systems [25,26,39–41]. Usually, the extrema of the Berry curvature are located at the corners of Brillouin zone. However, the maximum and the minimum values of the Berry curvature in our system are not at the exact corners of Brillouin zone. Figure 2(a) shows the Brillouin zone (Black solid lines) and the extrema of the Berry curvature in our system (Red dots). The extrema of the Berry curvature are not exactly at the corner of Brillouin zone, and four of

them are outside the first Brillouin zone. This discrepancy is caused by the mismatch between the asymmetrical spiral and the triangular lattice.

The detailed Berry curvatures around each K valley are presented in Fig. 2(b). The Berry curvature of the second band and the third band are enclosed by the cyan and magenta dotted boxes, respectively. The areas enclosed by these boxes represent the integral bound for the valley Chern number calculation mentioned above. Interestingly, numerical integration of the Berry curvature of our system provides the anomalous C_v about ± 0.33 that is not limited to ± 0.5. This may be caused by the strong spatial inversion symmetry breaking [12,32,42]. Further discussion follows next.

IV. SLOWNESS CURVES AND GROUP VELOCITY

The strong spatial inversion symmetry breaking in our spiral system is reflected on the distribution of slowness curves and group velocity, which is related to the Berry curvature by $\Omega(\mathbf{q}) = \pm \frac{m v_g^2}{2(|\mathbf{q}|^2 v_g^2 + m^2)^{\frac{3}{2}}}$, where v_g is the group velocity around the valley point, m is the strength of the spatial inversion breaking, and $\mathbf{q} = \mathbf{k} - \mathbf{k}_K$ is the wave vector deviation from the corresponding K point [27]. We evaluate the slowness
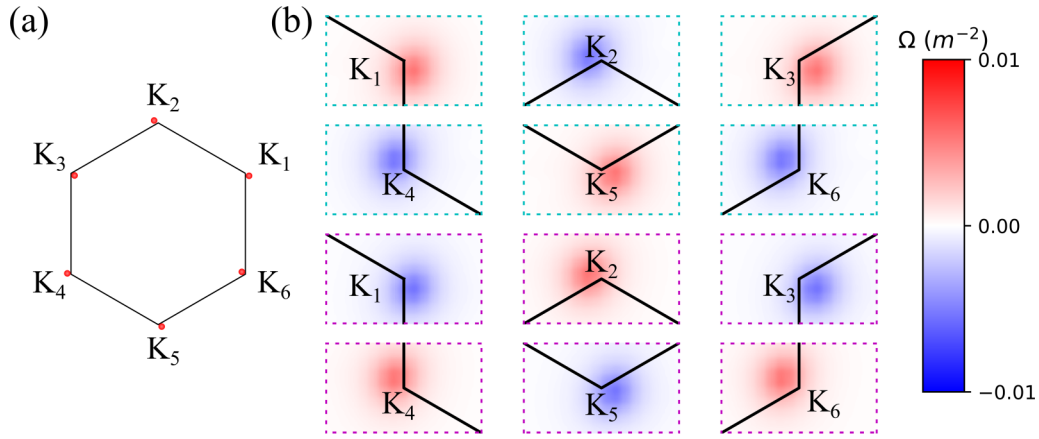
FIG. 2. (a) The black solid lines represent the Brillouin zone, while the red dots denote the extrema of the Berry curvature. (b) The detailed Berry curvature distribution near the six valleys for the second band (upper two rows enclosed by the cyan dotted boxes) and for the third band (lower two rows enclosed by the magenta dotted boxes). The color represents the amplitude of the Berry curvature (see the color map), and the black lines are the boundaries of the Brillouin zone. Given that the side length of the first Brillouin zone is S_{BZ}, the width of the area is $\frac{4\sqrt{3}}{15}S_{BZ}$, and the height of the area is $\frac{1}{5}S_{BZ}$.

curves and group velocities as a function of the wave vectors. Figures 3(a) and 3(b) present the polar plots of the slowness curves of the second band and the third band, showing the distribution of slowness magnitude for different directions in the first Brillouin zone. The slowness is the inverse of the phase velocity ($s = \frac{1}{v_p}$). The slowness curves corresponding to the second and third band are approximately circular at small wave vectors. We observe that the slowness curves exhibit the evident anisotropy as wave vectors increase. As
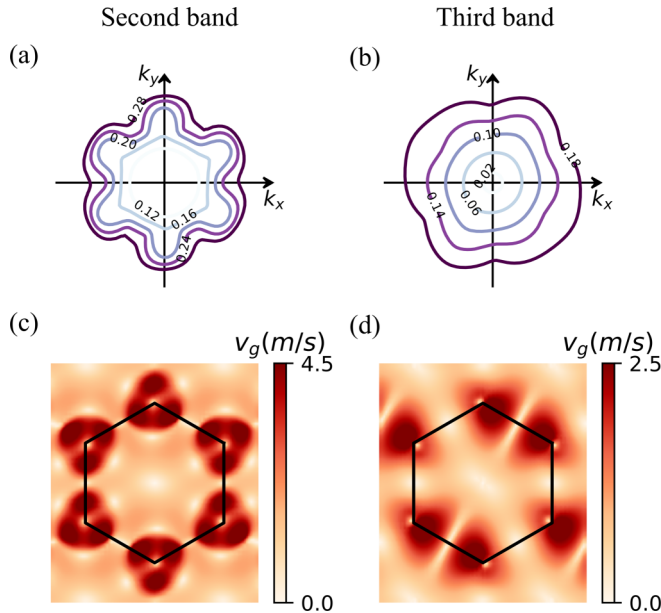

FIG. 3. (a) The slowness curves of the second band. From the small wave vectors to large wave vectors, the slowness rises from 0.12 to 0.28. (b) The slowness curves of the third band. From the small wave vectors to large wave vectors, the slowness rises from 0.02 to 0.18. (c) The group velocity distribution of the second band. The black solid line indicates the Brillouin zone. (d) The group velocity distribution of the third band. The black solid line indicates the Brillouin zone.

wave vectors increase, the values of the slowness of the second band and the third band rise, which is consistent with the corresponding band structures in Fig. 1(c). As the wave vector approaches the edges of the first Brillouin zone, the slopes of the corresponding bands decrease. It is noted that the slowness curves are symmetrical around the central point, which agrees with the band structures in Figs. 1(c) and 1(d).

The calculated group velocity distribution of the second and the third band are presented in Figs. 3(c) and 3(d), respectively. It can be found that the group velocity patterns of both bands are quite complex, especially at the corners of the Brillouin zone. The group velocity distribution of both bands as a function of wave vectors is symmetrical around the center of the Brillouin zone, suggesting the chiral anisotropic structure of the elastic valley metamaterials, which is in correspondence to the slowness curves.

At this point, we clearly observed the anisotropic characteristic of the elastic valleys in our system from: (i) the distorted area enclosed by the extrema of the Berry curvature, (ii) the different distributions of the Berry curvature around K_1, K_2, and K_3 valleys, and (iii) the distribution of slowness and the group velocity. We now move on to the tunability of this Berry curvature distribution next.

V. TUNABLE BERRY CURVATURE AND VALLEY CHERN NUMBER

The Berry curvature plays an important role in wave motions, resulting in appealing phenomena, such as valley-polarized transport. Thus, it is desirable to have more choices of the Berry curvature. We investigate the tunability of the Berry curvature as a function of the key geometrical parameters of the Archimedean spiral structure, such as the number of turns (n) and the thickness of the spiral (d) [Fig. 1(b)]. We calculate the Berry curvature and valley Chern number for $n = 1.5$ and $n = 2$ with the increase of d. For simplicity, we only show the Berry curvature around K_6 valley. The Berry curvatures and valley Chern numbers of the second band (enclosed by cyan dotted boxes) and the third band (magenta
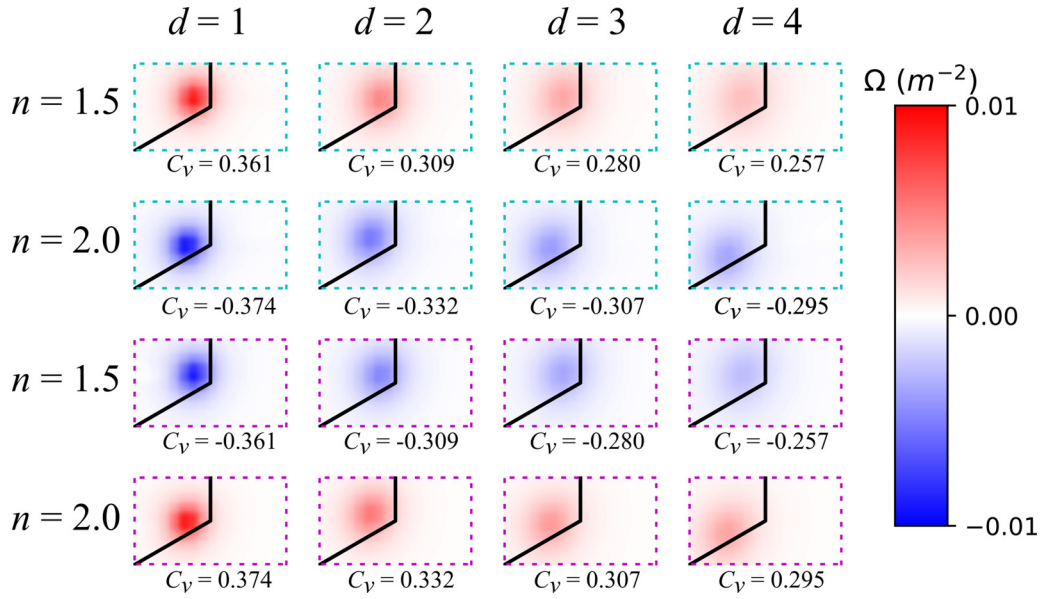
FIG. 4. The Berry curvature distributions around the K_6 point. Berry curvature distributions for the second band (upper two rows enclosed by the cyan dotted boxes) and for the third band (lower two rows enclosed by the magenta dotted boxes) are shown with different parameters. The color represents the amplitude of the Berry curvature (see the color map), and the black lines are the boundaries of the Brillouin zone. Given that the side length of the first Brillouin zone is S_{BZ}, the width of the area is $\frac{4\sqrt{3}}{15}S_{BZ}$, and the height of the area is $\frac{1}{5}S_{BZ}$.

boxes) are displayed in Fig. 4. We observe that as d increases, the magnitude of the Berry curvature becomes small and the distribution becomes dispersed. This is reasonable, since the Archimedean spiral approaches a circle with the increase of the thickness, thus resulting in the disappearance of the Berry curvature in the absence of the broken spatial inversion symmetry. Accordingly, the valley Chern number diminishes as displayed below each graph. When d is fixed, the increase of n from 1.5 to 2 can enhance the absolute value of the valley Chern number.

Figure 5 shows the Berry curvature along $K_6 K_1$ line at $n = 1.5$ and 2 (left and right panels) for various d values. In the case of the second band [Fig. 5(a)], we observe that the absolute value of the Berry curvature decreases as d increases. As the thickness of the Archimedean spiral is fixed, the sign of the Berry curvature changes when n changes from 1.5 to 2.0. This was also observed in Fig. 4 (compare the color between rows). This sign flip can be translated into the topological transition. The same phenomenon can be observed from Fig. 5(b), which shows the distributions of the Berry curvature of the third band. From this graph, we can also find the extrema of Berry curvature are not at the corner of Brillouin zone (vertical dashed lines in Fig. 5) as we mentioned in the last section.

VI. ELASTIC TOPOLOGICAL VALLEY EDGE STATES RELYING ON FREQUENCY

A. Projected band structure and eigenmodes

Based on the tunability of the Berry curvature, the next step is naturally to investigate the elastic topological valley edge state, which is regarded as one of the most significant manifestations of valley-polarized behaviors. According to the result in the previous section, we can tune the value of the Berry curvature around valleys by adjusting n and d [mm]. We

use the symbol $(n_1, d_1 | n_2, d_2)$ to denote the combination of the two different configurations of elastic valley metamaterials. We choose the combination of (1.5, 3) and (2, 2) for the investigation of elastic topological valley edge states due to their overlapped frequency range and opposite Berry curvatures. As shown in Fig. 6(a), the projected band along the $\mathbf{k_x}$ direction is calculated using the sandwich supercell $(2, 2 | 1.5, 3 | 2, 2)$.

Because the armchair interface is along the $\mathbf{k_x}$ direction, the x projection of two valleys with opposite topological charges will usually cancel out each other at $\mathbf{k_x} = 0$, resulting in the nontopological interface. It is evident that there are three bands independent of the bulk shown in gray. Here, the red line represents the edge states located at the interface between (2, 2) and (1.5, 3), while the blue lines represent the edge states located at the interface between (1.5, 3) and (2, 2). We note that the first band [lower blue line in Fig. 6(a)] is more similar to the bulk mode, while others are not, since this branch flattens out (i.e., becomes nondispersive) as the absolute value of $\mathbf{k_x}$ increases and also, the mode shape in the case of small amplitude of $\mathbf{k_x}$ resembles a bulk state of the spiral as shown in Fig. 6(b). On the other hand, the second blue line represents the edge state, which can be verified by its eigenmodes [see the modes corresponding to yellow and blue dots in Fig. 6(b)].

The projected band structure along the $\mathbf{k_y}$ direction is displayed in right panel of Fig. 6(a). The domain wall along the $\mathbf{k_y}$ direction is zigzag. The y projection of two valleys onto the domain wall is $k_y = \frac{2\pi}{3\sqrt{3}c}$ and $k_y = -\frac{2\pi}{3\sqrt{3}c}$, respectively. Because the difference of valley-projected Chern number is nonzero as shown in the distributions of topological charges in the insets of Fig. 6(a), the topological edge states are expected to appear along the zigzag interface within the bandgap as a result of the bulk-edge correspondence. Simulation results
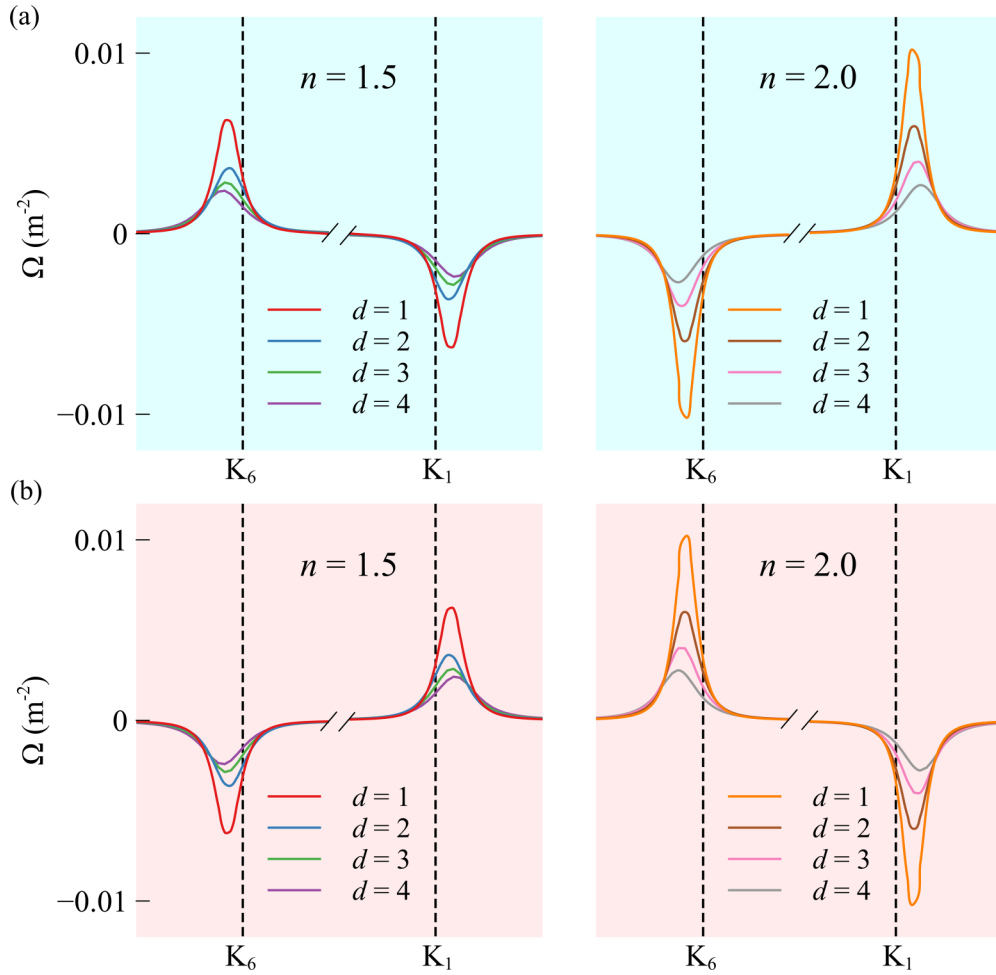
FIG. 5. (a) The Berry curvature of the second band along $K_6 K_1$ line as a function of the thickness of the Archimedean spiral, $d = 1, 2, 3$, and 4 [mm], when the number of turns of the spiral $n = 1.5$ and 2. (b) The same for the third band. Note that there is a broken x axis in each figure to emphasize the change of the Berry curvature in the K points.

clearly show two bands within the band gap, where the red line represents the topological edge states located at the interface between (2, 2) and (1.5, 3), while the blue line represents the topological edge states located at the interface between (1.5, 3) and (2, 2).

We also check the eigenmode of the edge states along the armchair and zigzag interface, respectively. Here we show the eigendisplacement fields of several **k** for comparison. For the projected band structure along the $\mathbf{k_x}$ direction, we choose $\mathbf{k_x} = 0.26$, where the eigenmodes are represented by red, olive, yellow circles, and $\mathbf{k_x} = 0.6$, where the eigenmodes are represented by green, cyan, and blue circles. As displayed in Fig. 6(b), the displacement field is mainly concentrated on the interface between two different elastic metamaterials. The intensity of eigenmode represented by the red circle is weaker than others. Besides, the vibration is mainly concentrated on the spiral rather than on the matrix in the eigenmode represented by the cyan circle. For the projected band structure along $\mathbf{k_y}$ direction, we choose $\mathbf{k_y} = 0.3$, where the eigenmodes are represented by magenta, orange circles, and $\mathbf{k_y} = 0.6$, where the eigenmodes are represented by black and teal circles. As displayed in Fig. 6(b), the displacement field is also concentrated on the interface between two different elastic

metamaterials. When the $\mathbf{k_y}$ approaches the origin, as shown in the eigenmode represented by the magenta and orange circles, the intensities of the edge modes at the interface are weaker than others.

B. Topological valley edge states

As discussed above, different interfaces can support distinctive edge states. Some studies have demonstrated the wave propagation along the domain wall characterized by 90° bends [12,43]. However, the results show the coupling behavior between armchair and zigzag interfaces varying case by case. Therefore, it is necessary to investigate the propagation of edge states along 90° bend in our system. Here, we create a two-part elastic metamaterial (see the insets of Figs. 7(b)–7(d) where green and red blocks represent (2, 2) and (1.5, 3) configurations, respectively), thereby forming four 90° channels. First, we calculate the transmission coefficient within the bandgap region from 155 to 160 Hz by using the ratio of input and output displacement [Fig. 7(a)]. The input and output are extracted by the displacement at the beginning of the armchair interface and at the bottom of the zigzag interface, respectively. Note that the frequency of the edge
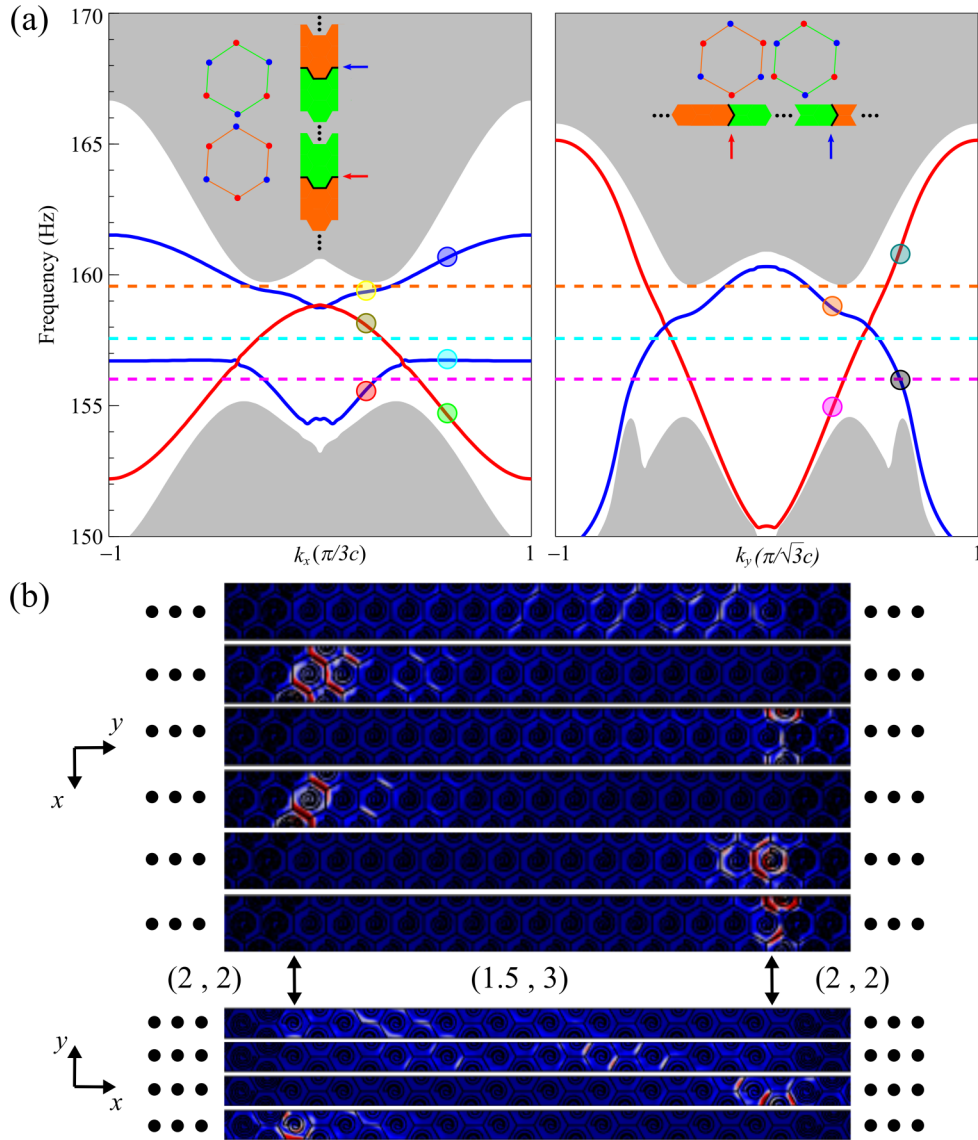
FIG. 6. (a) The projected band structures along the $\mathbf{k_x}$ (left panel) and $\mathbf{k_y}$ (right panel) directions. Several markers with different colors are shown in the topological band. For the projected band structure along the $\mathbf{k_x}$ direction, markers are placed on each topological band at $\mathbf{k_x} = 0.26$ and $\mathbf{k_x} = 0.6$. For the projected band structure along the $\mathbf{k_y}$ direction, markers are placed on each topological band at $\mathbf{k_y} = 0.3$ and $\mathbf{k_y} = 0.6$. The schematics of supercell setup are displayed as the inset where green blocks are (2, 2) and orange block are (1.5, 3). The topological charges distributions and the area enclosed by the extrema of Berry curvatures are shown in the inset. (b) The eigendisplacement fields corresponding to the markers indicated. The setup of sandwich supercell is shown by the notation we mention in the main text.

states within the bandgap along the $\mathbf{k_x}$ direction [red lines in Fig. 6(a)] is from 155 to 159 Hz, which can be divided into two regions shown in yellow and purple according to the value of transmission coefficient. Usually, armchair interfaces do not support the topological edge states and the valley states appear near $\mathbf{k_x} = 0$. However, in our elastic metamaterial, the Berry curvature distribution is deviated from the corners of the Brillouin zone, resulting in the nonoverlapping of positive and negative topological charges of two valleys [see the inset of Fig. 6(a)]. Besides, the magnitudes of topological charges are different as a result of the different valley Chern number (see Fig. 4). It will extend the region that exists valley states and reduce the intervalley scattering due to the disappearance of tiny gap that usually appears at $\mathbf{k_x} = 0$. Therefore, when the frequency is low, the valley state along armchair interface

cannot couple with the one along zigzag interface, and the transmission becomes low. However, when the frequency is high, they can couple well so that the transmission becomes high. When the frequency increases to 159 Hz and above, the transmission is low since the bandgap for edge states appears.

We then demonstrate a frequency selector using this property in our system. Figures 7(b)–7(d) show the schematics of the numerical setup (insets) and the simulation results. In Fig. 7(b), when the vibration source with 156 Hz [marked in the magenta line in Figs. 6(a), 6(b), and 7(a)] is set at the beginning of the interface between (2, 2) and (1.5, 3), we know that the edge modes shown in the red line in Fig. 6(a) can be excited based on the projected band structure along the $\mathbf{k_x}$ and $\mathbf{k_y}$ directions. The elastic waves will transport along the
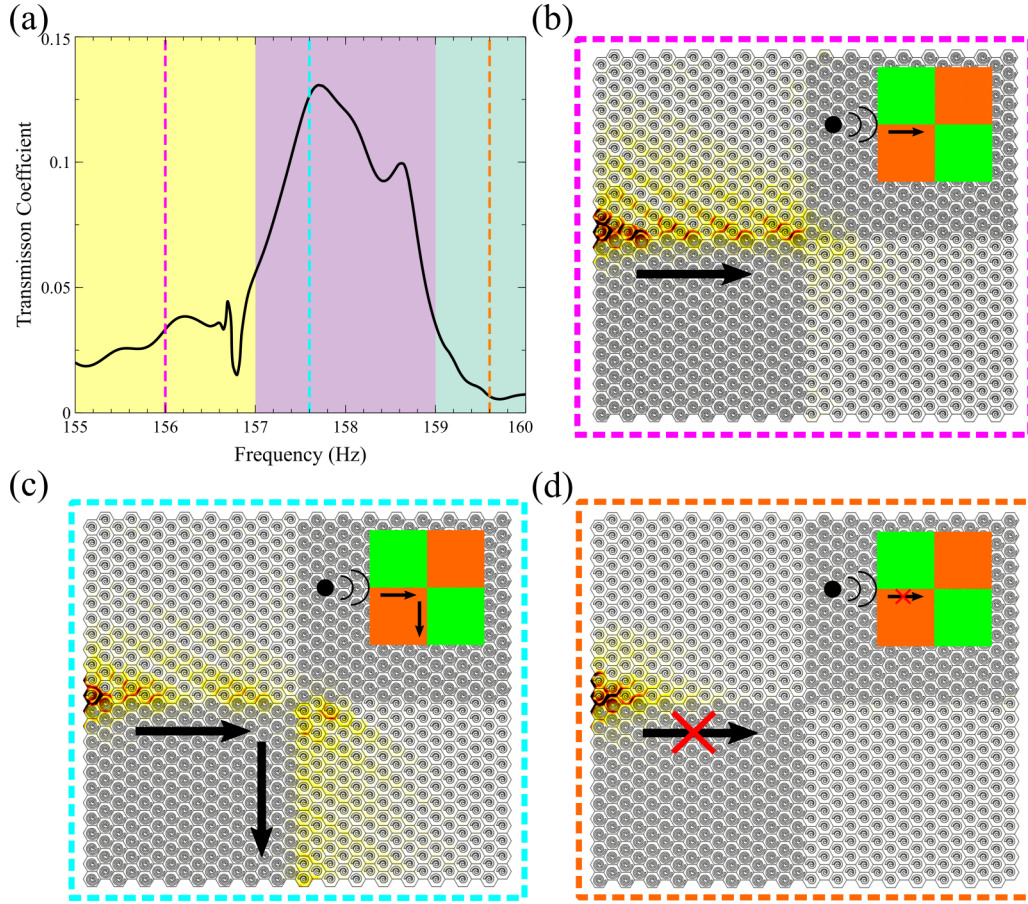
FIG. 7. (a) The transmission coefficient as a function of the frequency within the band gap. The yellow and purple represent the region with edge states. The pink region is the band gap between edge states and bulk states. The dashed lines with different colors represent the frequencies we choose to demonstrate the elastic wave propagation. (b) The transport of elastic waves along the interface. At the frequency of 156 Hz, which is shown in magenta dashed line in Figs. 6(a) and 6(b), elastic waves can travel along the $\mathbf{k_x}$ direction but cannot travel through the bend. (c) At the frequency of 157.6 Hz, which is shown in cyan dashed line in Figs. 6(a) and 6(b), elastic waves can travel along the path and through the bend. (d) At the frequency of 159.6 Hz, which is shown in orange dashed line in Figs. 6(a) and 6(b), elastic waves cannot propagate. The insets of (b), (c), and (d) show the schematics of the numerical setup, where the green blocks represent (1.5, 3) metamaterials and the orange blocks represent (2, 2) metamaterials.

interface in the x direction. However, when the direction is changed to the $\mathbf{k_y}$ direction, the edge mode cannot support the energy transfer along the vertical interface.

However, when the excitation frequency is high, such as 157.6 Hz [marked in the cyan line in Figs. 6(a), 6(b), and 7(a)], the transport of the elastic waves is distinct from the former case. As displayed in Fig. 7(c), when the elastic waves arrive at the intersection, they will not go forward but will propagate downward into another interface. The reason is evident. Edge modes in different interfaces belong to different valleys, and they cannot couple with each other. Thus, the excited edge modes cannot propagate forward after the intersection point. However, the downward edge mode and the excited mode are projected by the same valley. Therefore, when the elastic waves arrive at the intersection, they will neither go forward nor bisect into another interface, but go downward [22].

When we continue to increase the frequency, the displacement field with excitation frequency 159.6 Hz is shown in Fig. 7(d). Because of the band gap, elastic waves are trapped at the beginning of the interface. This property that edge states transport depending on frequency may have potential

applications in signal processing and frequency selector. However, the applicability of our system can be limited by a narrow bandgap observed in our two-dimensional model based on the plane strain condition. To obtain a larger bandgap, optimization of the material or extending the model to three-dimensional architectures may be required.

VII. CONCLUSIONS

The valley anisotropy is introduced by designing asymmetrical elastic metamaterials made of spiral structure and soft material. By numerical calculations, we reveal the unique anisotropic valley properties in our system, stemming from the deviated Berry curvature. The adjustment of the geometrical parameters in the spirals allows an extreme tunability of the Berry curvature. We exploit this to demonstrate the formation of valley topological states and topological band structures unprecedented in conventional topological platforms. Lastly, we show a special topologically protected transport of elastic waves in this platform of anisotropic elastic metamaterial.
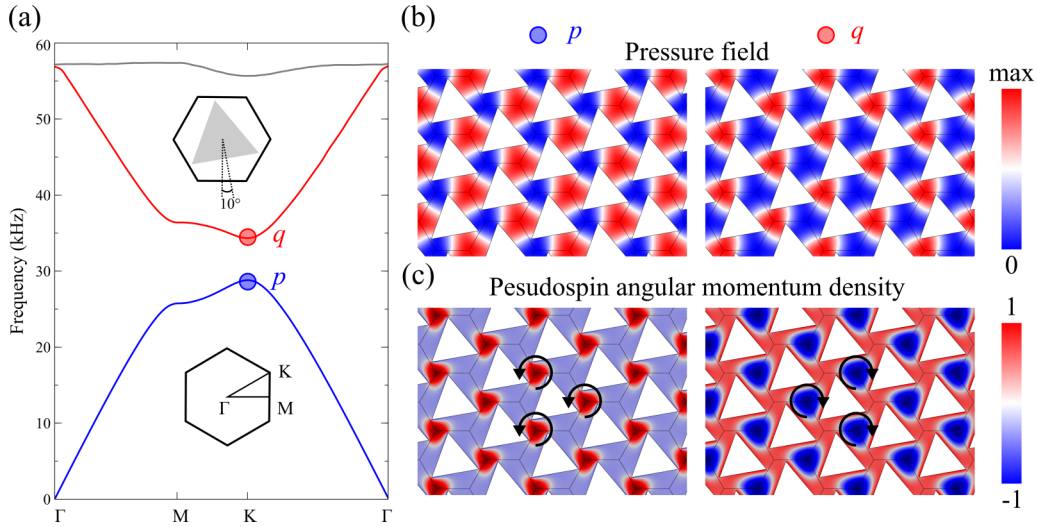
FIG. 8. (a) The band structure along Γ-M-K-Γ of the acoustic valley metamaterial for comparison. The blue, red, and gray curves represent the first, second, and third bands, respectively. (b) The amplitude distributions of pressure fields of the p and q states. (c) The normalized pseudospin angular momentum density of the p and q states.

The observed anomalous valley states enrich the intrinsic physics of the valley states. The deviated Berry curvature in the proposed elastic system may inspire similar explorations in other systems, such as electronic and photonic systems. The discussed elastic waves with valley anisotropic characteristics are transverse waves, which can exhibit superb penetration into soft media. Thus, the hydrogel-based transverse wave manipulator can be glued to a variety of media including hard and soft, leading to potential biomedical applications, e.g., elastography.

APPENDIX: COMPARISON BETWEEN TRADITIONAL ACOUSTIC VALLEY METAMATERIALS AND OUR METAMATERIALS

Here, we show the distinctive landscape of valley vortex states of our system in comparison to that of conventional val-

ley metamaterials. To this end, we use one of the most widely studied acoustic valley systems [see the inset of Fig. 8(a)], consisting of equilateral triangular rods arranged in a triangular lattice in water [28,44,45]. The equilateral triangular rod is made of steel with $\rho = 7670 \, \text{kg/m}^3$, $c_p = 6010$ m/s, $c_s = 3230$ m/s, and the acoustic parameters for water are $\rho = 1000 \, \text{kg/m}^3$, $c_p = 1490$ m/s. The lattice constant is $14\sqrt{3}$ mm, and the side of equilateral triangular rod is 20 mm. When the symmetries between the lattice and scatterer match, the Dirac cone is expected to appear at the K point. In order to open the Dirac cone, we need to break the spatial inversion symmetry by rotating the steel rod. Here the rotation angle is $10°$ as shown in the inset of Fig. 8(a).

Figure 8(a) shows the band structure of this acoustic metamaterial. The Brillouin zone and the high symmetrical points are shown in the inset. Clearly, there is a band gap around 30 kHz, and the band structure shows two extrema at the K point, which are denoted as p and q states, respectively. To show the valley features, we investigate the eigenpressure field and pseudospin angular momentum density distribution similar to what we have done in our main text. As displayed in Figs. 8(b) and 8(c), when the eigenpressure fields reach a maximum in the corners of hexagon in both p and q states, the pseudospin angular momentum densities tend to be zero. We also notice that the p state is in the pseudospin up state and the local particle velocity rotates counterclockwise, while the q state is the opposite. In sharp contrast, in our system as shown in Figs. 1(e) and 1(f), when the eigenfields reach maximum in the corners of the hexagon in both p and q states, the amplitudes of pseudospin angular momentum densities also tend to be maximum.

[1] Y. K. Mariappan, K. J. Glaser, and R. L. Ehman, Clin. Anat. **23**, 497 (2010).

[2] B. S. Garra, Abdom. Imaging **40**, 680 (2015).

[3] D. M. Kochmann, J. A. Lewis, C. Daraio, J. R. Raney, N. Nadkarni, and K. Bertoldi, Proc. Natl. Acad. Sci. **113**, 9722 (2016).

[4] P. Grasland-Mongrain, R. Souchon, F. Cartellier, A. Zorgani, J. Y. Chapelon, C. Lafon, and S. Catheline, Phys. Rev. Lett. **113**, 038101 (2014).

[5] M. Miniaci, A. S. Gliozzi, B. Morvan, A. Krushynska, F. Bosia, M. Scalerandi, and N. M. Pugno, Phys. Rev. Lett. **118**, 214301 (2017).

[6] A. Spadoni and C. Daraio, Proc. Natl. Acad. Sci. **107**, 7230 (2010).

[7] M. Carrara, M. R. Cacan, J. Toussaint, M. J. Leamy, M. Ruzzene, and A. Erturk, Smart Mater. Struct. **22**, 065004 (2013).

[8] J.-W. Dong, X.-D. Chen, H. Zhu, Y. Wang, and X. Zhang, Nat. Mater. **16**, 298 (2016).

[9] X.-D. Chen, W.-M. Deng, J.-C. Lu, and J.-W. Dong, Phys. Rev. B **97**, 184201 (2018).

[10] C. He, X. Ni, H. Ge, X.-C. Sun, Y.-B. Chen, M.-H. Lu, X.-P. Liu, and Y.-F. Chen, Nat. Phys. **12**, 1124 (2016).

[11] T.-W. Liu and F. Semperlotti, Phys. Rev. Appl. **9**, 14001 (2018).

[12] H. Zhu, T.-W. Liu, and F. Semperlotti, Phys. Rev. B **97**, 174301 (2018).

[13] J. Petersen, J. Volz, and A. Rauschenbeutel, Science **346**, 67 (2014).

[14] K. Y. Bliokh, D. Smirnova, and F. Nori, Science **348**, 1448 (2015).

[15] J. Lin, J. P. B. Mueller, Q. Wang, G. Yuan, N. Antoniou, X. C. Yuan, and F. Capasso, Science **340**, 331 (2013).

[16] A. B. Young, A. C. T. Thijssen, D. M. Beggs, P. Androvitsaneas, L. Kuipers, J. G. Rarity, S. Hughes, and R. Oulton, Phys. Rev. Lett. **115**, 153901 (2015).

[17] S. Li, D. Zhao, H. Niu, X. Zhu, and J. Zang, Nat. Commun. **9**, 1370 (2018).

[18] M. Miniaci, R. K. Pal, B. Morvan, and M. Ruzzene, Phys. Rev. X **8**, 031074 (2018).

[19] L. M. Nash, D. Kleckner, A. Read, V. Vitelli, A. M. Turner, and W. T. M. Irvine, Proc. Natl. Acad. Sci. **112**, 14495 (2015).

[20] R. Süsstrunk and S. D. Huber, Science **349**, 47 (2015).

[21] K. H. Matlack, M. Serra-Garcia, A. Palermo, S. D. Huber, and C. Daraio, Nat. Mater. **17**, 323 (2018).

[22] M. Yan, J. Lu, F. Li, W. Deng, X. Huang, J. Ma, and Z. Liu, Nat. Mater. **17**, 993 (2018).

[23] H. Chen, H. Nassar, and G. L. Huang, J. Mech. Phys. Solids **117**, 22 (2018).

[24] R. Chaunsali, C.-W. Chen, and J. Yang, Phys. Rev. B **97**, 054307 (2018).

[25] J. Vila, R. K. Pal, and M. Ruzzene, Phys. Rev. B **96**, 134307 (2017).

[26] R. K. Pal and M. Ruzzene, New J. Phys. **19**, 025001 (2017).

[27] D. Xiao, W. Yao, and Q. Niu, Phys. Rev. Lett. **99**, 236809 (2007).

[28] J. Lu, C. Qiu, M. Ke, and Z. Liu, Phys. Rev. Lett. **116**, 093901 (2016).

[29] X. Xu, W. Yao, D. Xiao, and T. F. Heinz, Nat. Phys. **10**, 343 (2014).

[30] K. F. Mak, K. L. McGill, J. Park, and P. L. McEuen, Science **344**, 1489 (2014).

[31] A. Rycerz, J. Tworzydło, and C. W. J. Beenakker, Nat. Phys. **3**, 172 (2007).

[32] I. Kim, Y. Arakawa, and S. Iwamoto, Appl. Phys. Express **12**, 047001 (2019).

[33] M. Miniaci, R. K. Pal, R. Manna, and M. Ruzzene, Phys. Rev. B **100**, 024304 (2019).

[34] J. M. Kweun, H. J. Lee, J. H. Oh, H. M. Seung, and Y. Y. Kim, Phys. Rev. Lett. **118**, 205901 (2017).

[35] J.-Y. Sun, X. Zhao, W. R. K. Illeperuma, O. Chaudhuri, K. H. Oh, D. J. Mooney, J. J. Vlassak, and Z. Suo, Nature **489**, 133 (2012).

[36] O. Isik and K. P. Esselle, Metamaterials **3**, 33 (2009).

[37] Y. Long, J. Ren, and H. Chen, Proc. Natl. Acad. Sci. **115**, 9951 (2018).

[38] T. Fukui, Y. Hatsugai, and H. Suzuki, J. Phys. Soc. Jpn. **74**, 1674 (2005).

[39] F. Zhang, A. H. MacDonald, and E. J. Mele, Proc. Natl. Acad. Sci. **110**, 10546 (2013).

[40] X.-D. Chen, F.-L. Zhao, M. Chen, and J.-W. Dong, Phys. Rev. B **96**, 020202 (2017).

[41] T. Ma and G. Shvets, New J. Phys. **18**, 25012 (2016).

[42] K. Qian, D. J. Apigo, C. Prodan, Y. Barlas, and E. Prodan, Phys. Rev. B **98**, 155138 (2018).

[43] Y. Yang, Z. Yang, and B. Zhang, J. Appl. Phys. **123**, 091713 (2018).

[44] L. Ye, C. Qiu, J. Lu, X. Wen, Y. Shen, M. Ke, F. Zhang, and Z. Liu, Phys. Rev. B **95**, 174106 (2017).

[45] J. Lu, C. Qiu, L. Ye, X. Fan, M. Ke, F. Zhang, and Z. Liu, Nat. Phys. **13**, 369 (2017).